# SUPPORTING INFORMATION

## Structural Dynamics of Bismuth Triiodide in Solution Triggered by Photoinduced Ligand-to-Metal Charge Transfer

Eun Hyuk Choi,[†,‡,Δ] Doo-Sik Ahn,[†,‡,Δ] Sungjun Park,[†,‡] Changwon Kim,[†,‡] Chi Woo Ahn,[†,‡] Siin Kim,[†,‡] Minseo Choi,[†,‡] Cheolhee Yang,[‡] Tae Wu Kim,[‡] Hosung Ki,[‡] Jungkweon Choi,[†,‡] Martin Nors Pedersen,[§] Michael Wulff,[§] Jeongho Kim,[#] and Hyotcherl Ihee[*,†,‡]

[†]Department of Chemistry and KI for the BioCentury, Korea Advanced Institute of Science and Technology (KAIST), Daejeon 34141, Republic of Korea

[‡]Center for Nanomaterials and Chemical Reactions, Institute for Basic Science (IBS), Daejeon 34141, Republic of Korea

[#]Department of Chemistry and Chemical Engineering, Inha University, 100 Inha-ro, Nam-gu, Incheon, 22212, Republic of Korea

[§]European Synchrotron Radiation Facility (ESRF), 38000 Grenoble Cedex 9, France

[Δ]These authors equally contributed to this work

[*]Corresponding author. E-mail: hyotcherl.ihee@kaist.ac.kr

# Table of Contents

**1. Details of Time-Resolved X-ray Liquidography (TRXL) experiment**

The TRXL experiment was conducted at the ID09 beamline of the European Synchrotron Radiation Facility (ESRF). Details of TRXL setup were reported elsewhere.[S1,2] Briefly, the pump-probe scheme was applied to monitor the time-dependent X-ray scattering signals upon irradiation with an optical laser pulse. Optical laser pulses with the center wavelength of 400 nm were generated by second harmonic generation (SHG) of the 800-nm femtosecond laser pulses, which were provided by an 1-kHz amplified Ti:sapphire laser system, and was used as pump to initiate the photochemical reaction. The optical laser pulses were temporally stretched to ~2 ps by passing through an additional dispersive material (fused silica) to prevent multiphoton excitation. The 400 nm optical laser pulses have the energy of 95 mJ/pulse and were focused to a 0.23 (width) × 0.29 (height) mm$^2$ spot at the sample position, providing a fluence of ~1.8 mJ/mm$^2$. After initiating the reaction by the optical laser pulse, a time-delayed X-ray pulse was delivered to the sample to probe the reaction dynamics. The ~100 ps-long X-ray pulses with the center energy of 18 keV and the energy bandwidth of $\Delta E/E$ = ~0.9% were generated by diffracting the white X-ray pulses from the U17 undulator through Ru multilayer optics. A single X-ray pulse was selected from the 4-bunch (4 × 10) filling mode of the storage ring by a synchronized mechanical chopper and focused to a 0.172 (width) × 0.108 (height) mm$^2$ spot at the sample position. The scattered X-ray photons by the sample solution were collected by an area detector (Rayonix MX170-HS, 1920 × 1920 pixels, 89 mm pixel size) in 2 × 2 binning mode with a sample-to-detector distance of 45 mm and an exposure time of three seconds per image. The sample solution of 1.0 mM BiI$_3$ (Aldrich, 99%) in acetonitrile (Aldrich, anhydrous, 99.8%) was circulated through a quartz capillary nozzle of 500 μm thickness. The open jet capillary system with the thickness of 500 μm provides a stable flow of liquid with a speed fast enough to deliver fresh sample solution at every pump-probe measurement at a repetition rate of 1 kHz. We obtained the solution scattering signals at the pump-probe time delays of t = −3 ns, 100 ps, 178 ps, 316 ps, 562 ps, 1 ns, 1.78 ns, 3.16 ns, 5.62 ns, 10 ns, 56.2 ns, 100 ns and 1 μs. The difference scattering signals, $\Delta S(q, t)$, were obtained by subtracting the scattering signal from unexcited sample, measured at a negative time delay ($t = −3$ ns), from the signals measured at positive time delays.

**2. Details of data processing, data analysis, density functional theory calculation and molecular dynamics simulation**

**Data Processing.** The two-dimensional scattering images were transformed into one-dimensional scattering curves via azimuthal integration as a function of the momentum transfer $q = (4\pi/\lambda)\sin(2\theta/2)$, where $\lambda$ is the wavelength of X-rays and the $2\theta$ is the scattering angle, and the time delay t. The scattering curves were normalized by the area under the curve at $q$ values from 4.0 to 8.0 Å$^{-1}$. After normalization, the difference scattering curves were obtained by subtracting the scattering curve at a negative time delay (t = –3 ns) from the scattering curves at positive time delays. The difference scattering curves were further scaled to the unperturbed scattering intensity of one acetonitrile molecule so that the scattering intensity have an absolute scale corresponding to one solvent molecule. The difference radial intensity, $r^2\Delta R(r, t)$, represents the change of radial electron density as a function of interatomic distance $r$ in real space, and was obtained by sine-Fourier transform of the $q\Delta S(q, t)$ curves with the following relation:

$$r^2\Delta R(r, t) = \frac{r}{2\pi^2} \int_0^\infty q\Delta S(q)\sin(q, t)e^{-q^2\alpha}\, dq \tag{S1}$$

The Gaussian damping factor $\alpha = 0.03$ Å$^2$ was employed to account for the finite experimental $q$-range of our measurement.

**Data Analysis.** Time-resolved X-ray solution scattering curves were analyzed by global fit method using a home-made algorithm. In the global fit analysis, the experimental scattering curves (in the $q$ range from 0.7 to 9.0 Å$^{-1}$) were fit against theoretical scattering curves by minimizing the sum of reduced-$\chi^2$ values of the difference between experimental and theoretical curves at all positive time delays:

$$\chi^2 = \frac{1}{N - p - 1} \sum_{j=\text{time delay}} \sum_i \frac{(\Delta S_{\text{theory}}(q_i, t_j) - \Delta S_{\text{experiment}}(q_i, t_j))^2}{\sigma_{i,j}^2} \tag{S2}$$

where $N$ is the total number of data points along the $q$ axis, $p$ is the number of fit parameters and $\sigma_{i,j}$ is the standard deviation of the difference scattering intensity at $i^{\text{th}}$ $q$ of $j^{\text{th}}$ time delay. From the global fit analysis, we globally determined a total of fifteen fit parameters, including the reaction rate constants and branching ratios of the photoproducts, the excitation ratio of the photoexcited molecules, and various structural parameters of solute molecules. The $\chi^2$ minimization was performed using the MINUIT package written at CERN and the error analysis was done by MINOS, a built-in algorithm in the MINUIT software.[S3] The theoretical

difference scattering curves can be described by three terms: (i) solute-only term, (ii) cage tem (solute-solvent cross term) and (iii) solvent-only term. The solute-only term can be calculated by the well-known Debye equation based on the optimized structures of solute molecules. The structures of possible photoproducts and ground-state $BiI_3$ were initially optimized with DFT calculations, and those starting structures were modified during the global fit analysis to improve the fit qualities. Briefly, the structure modification of ground-state $BiI_3$ and $BiI_2\cdot$ was performed in Cartesian coordinates while that of $iso$-$BiI_2$-I was carried out in Z-matrix and the resultant internal coordinate information was transformed back into Cartesian coordinates to obtain the atomic pair distances. In particular, the three Bi-I bond lengths of ground state $BiI_3$ were adjusted using two independent parameters with other structural configurations fixed. For $BiI_2\cdot$, the two Bi-I bond lengths and one I-Bi-I angle were adjusted using two independent parameters. For $iso$-$BiI_2$-I, the two Bi-I bond lengths, one I-I bond, one I-Bi-I angle, one Bi-I-I angle and one I-Bi-I-I dihedral angle were modified using five independent parameters. The structure of $I_2$ was used as it was obtained from DFT calculation. For the cage term, an MD simulation was performed for each solute structure and the corresponding RDF was calculated, from which the scattering intensity of the cage term was obtained. For the solvent-only term, we have previously demonstrated that it is possible to measure the solvent heating signals experimentally and that the fit quality for TRXL data can be greatly improved when we use experimentally determined solvent heating signals rather than those obtained theoretically from MD simulations.[S4] Hence, we generally perform an extra measurement of solvent heating to obtain $(\partial S(q)/\partial T)_\rho$ and $(\partial S(q)/\partial \rho)_T$, which constitute the solvent-only difference scattering signal. The theoretical difference scattering curves were constructed by combining the three terms as follows:

$$\Delta S(q,\,t) = \Delta S_{solute}(q,\,t) + \Delta S_{cage}(q,\,t) + \Delta S_{solvent}(q,\,t)$$

$$= \Delta S_{solute\text{-}related}(q,\,t) + \Delta S_{solvent}(q,\,t)$$

$$= \frac{1}{R}\left[\sum_k c_k(t)S_k(q) - S_g(q)\sum_k c_k(0)\right] + \left[\left(\frac{\partial S}{\partial T}\right)_\rho \Delta T(t) + \left(\frac{\partial S}{\partial \rho}\right)_T \Delta \rho(t)\right]$$

(S3)

where $R$ is the number ratio of the solvent molecules to solute molecules, $k$ is the index of the solute species (reactants, intermediates and products), $c_k(t)$ is the fractional concentration of $k^{th}$ species at time delay $t$, $S_k(q)$ is the solute-related (that is, solute-only and cage terms)

scattering curve of $k^{th}$ species, and $S_g(q)$ is the scattering curve of the ground state reactant. The temperature and density changes, $\Delta T(t)$ and $\Delta\rho(t)$, were obtained by solving the hydrodynamics equations, in which the heat released during the entire course of reaction was estimated based on the excitation energy, quantum yield, and relative energies of intermediates and products with respect to the ground-state reactant. More details of how to solve hydrodynamics equations are described in the following section. The time dependent concentrations of the intermediate and product species were calculated by numerically solving a set of differential equations derived from the assumed model kinetic scheme.

**Density Functional Theory Calculation.** The ground-state structure of $BiI_3$ and the structures of candidate intermediates in the $S_0$ states were obtained from density functional theory (DFT) calculations using the CAM-B3LYP functional with def2-TZVP basis sets. For the geometry optimization in the $S_1$ state, time-dependent DFT (TDDFT) calculations were carried out. Solvent effects for acetonitrile were implicitly included by applying the conductive polarizable continuum model (CPCM) for all the calculations.[S5] The optimized stationary and transition state structures in $S_0$ and $S_1$ states were confirmed by the vibrational normal mode analysis. All calculations were performed using the Gaussian 16 (version B.01) software.[S6]

**Molecular Dynamics Simulation.** Molecular dynamics (MD) simulation was performed using the MOLDY program to obtain the cage terms for all the chemical species involved in the reaction.[S7] One solute molecule was embedded in 512 acetonitrile solvent molecules in a virtual cubic box of ~35.7 Å size. The internal structure of each molecule was fixed and the intermolecular interactions were governed by Coulomb forces and Lennard-Jones potentials. The NBO atomic charges obtained from DFT calculations and universal force field (UFF) parameters were used to describe the intermolecular interactions.[S8] All simulations were performed at an ambient temperature of 300 K with a solvent density of 0.786 $g/cm^3$. The system was equilibrated over 20 ps via coupling to a Nose-Hoover thermostat.[S9] The simulations were performed in the NVT ensemble with a time step of 5 fs and the trajectories were followed up to 500 ps. From the simulation, we obtained the RDFs, from which the scattering intensity of the cage term was calculated.

## 3. Decomposition of solution scattering signal, $q\Delta S(q, t)$ and $r^2\Delta R(r, t)$

The difference scattering curves of $BiI_3$ in solution shown in Figure 2 can be decomposed into three contributions: (i) solute-only term, (ii) cage term and (iii) solvent-only term. As we described in the main text, the solute-only term was calculated with the Debye equation. For the cage term, we obtained radial distribution functions (RDFs) of every atomic pair in a virtual box containing one solute molecule embedded in 512 solvent molecules from molecular dynamics (MD) simulation and then extracted the RDFs corresponding to the solute-solvent intermolecular atomic pairs, from which $q\Delta S(q, t)$ of the cage term was derived. The solute-only $q\Delta S(q, t)$ is a sum of the Debye scattering curves of all the solute species while the cage term of $q\Delta S(q, t)$ is a sum of the scattering signals arising from all of the cage structures, each of which includes the individual solute species. Therefore, the intensities and shapes of both the solute-only and cage scattering curves change over time following the concentration profiles of the solute species. The decomposed time-resolved scattering curves are shown in Figure S2.

The time-dependent behaviour of the solvent-only term is determined by the temperature and density changes induced by the photoreaction, as can be seen in Equation (3) in the main text. Thus, we need to estimate the temperature and density changes as a function of time, $t$. To achieve this goal, we first estimated the heat (in the unit of J/mol), $Q(t)$, released to the solvent as a function of time by using the following equation:

$$Q(t) = \text{Energy}(t = 0) - \text{Energy}(t)$$

$$= \frac{N_A}{R} f_{exc} \left[ \sum_k (E_g + h\upsilon)c_k(0) - \sum_k E_k c_k(t) \right] \tag{S4}$$

$$+ \frac{N_A}{R} f_{exc} f_{fast} \left[ 1 - \exp(-t/k_{fast}) \right]$$

where $N_A$ is Avogadro's number, $R$ is the ratio of the number of solvent molecules to that of solute molecules, $c_k(t)$ is the unitless fractional concentration of species $k$ at time $t$, $E_g$ is the absolute energy of the ground-state molecule in the unit of J/molecule, $h\upsilon$ is the excitation energy, $E_k$ is the energy of species $k$, $f_{exc}$ is the ratio of initial excitation, $f_{fast}$ is the ratio of fast-decaying population through vibrational cooling, and $k_{fast}$ is the rate constant for vibrational

cooling. The absolute energy of each species was determined by DFT/TDDFT calculations. Here, the cooling rate $k_{fast}$ is assumed to be $(5\text{ ps})^{-1}$. Since the vibrational cooling process occurs much faster than our temporal resolution of 100 ps, the same heat $Q(t)$ in Equation (S4) can be obtained at $t \geq 100$ ps regardless of the value of $k_{fast}$ as long as it is much larger than $(100\text{ ps})^{-1}$.

Then, based on the obtained $Q(t)$, we calculated the changes of pressure $\Delta P(t)$, temperature $\Delta T(t)$, and density $\Delta \rho(t)$ by solving the following hydrodynamics equations:

$$\Delta P(t) = \frac{\alpha_P}{\chi_T C_V} \int_{-\infty}^{t} \frac{\partial Q}{\partial t}(\tau) \exp[-\{(\frac{v_s}{a})(t-\tau)\}^2]d\tau$$

$$\Delta T(t) = \frac{Q(t) - (C_V - C_P)\frac{\chi_T}{\alpha_P}\Delta P(t)}{C_P} \tag{S5}$$

$$\Delta \rho(t) = \rho_0[\chi_T \Delta P(t) - \alpha_P \Delta T(t)]$$

where $\alpha_P$ in the unit of $K^{-1}$ is the isobaric thermal expansion coefficient, $\chi_T$ in the unit of $Pa^{-1}$ is the isothermal compression coefficient, $v_s$ in the unit of m/s is the speed of sound in the solvent, $a$ in the unit of m is the root-mean-square size of a laser spot, $C_V$ in the unit of $J\text{ mol}^{-1}\text{ K}^{-1}$ is the heat capacity at constant volume, and $C_P$ is the heat capacity at constant pressure. The estimated changes of temperature and density are shown in Figure S4. According to Equation (S3), now it is possible to calculate the solvent-only scattering signal as a function of time and the resultant curves are presented in Figure S2.

The three components constituting the theoretical curves can be converted into the difference radial intensities, $r^2\Delta R(r, t)$, via sine-Fourier transform using Equation (S1), as shown in Figure S3. Each of the decomposed $r^2\Delta R(r, t)$ in Figure S3 is the real-space representation of the theoretical $q\Delta S(q, t)$ curves in Figure S2 and contains direct structural information in the form of atomic pair distances. The newly generated and depleted atomic pair distances are represented as vertical upward and downward bars, respectively, at the bottom of each plot.

## 4. Experimental solute-only $r^2\Delta R(r, t)$

For each of the four candidate pathways shown in Figure 3, we constructed a theoretical difference scattering curve and fit it to the experimental scattering curve in $q$-space by optimizing time-dependent concentrations of transient intermediate and product species as well as the contribution of solvent heating (Figure S4) as described in the previous section. From the experimental scattering curve and its theoretical fit, we extracted the experimental solute-only terms by subtracting the cage and solvent-only terms, which were obtained from a MD simulation and a separate TRXL experiment for a dye in solution, respectively. Then, by sine-Fourier transform of the solute-only terms in $q$-space, experimental $r^2 \Delta R_{solute}(r)$ can be obtained.


## 5. SVD analysis of experimental, theoretical and mock data

Singular value decomposition (SVD) is a mathematical procedure for matrix factorization and often employed in time-resolved studies including spectroscopy and X-ray diffraction/scattering.[S10-12] By applying SVD to the high-$q$ region of our data where the solute-only term dominates, we factored our experimental and theoretical data matrices whose rows and columns are in the domains of momentum transfer vector $q$ and time $t$, respectively. The resultant right singular vectors (RSVs) of the experimental and theoretical data are shown in Figure S5. We can see that both of the experimental and theoretical RSVs can be well described with a sum of two exponential functions, even though the fit curves for the experimental and theoretical RSVs still show deviations from each other. This is mainly due to the noisy nature of signal in the high-$q$ region, where some detailed signal features are obscured. When we apply SVD to the data in the entire $q$-range, both experimental and theoretical data give almost identical RSVs and fit curves (data not shown).

The left singular vectors (LSVs) of the experimental and theoretical data are shown in Figures S6(d) and S6(e), respectively. For solute-only terms, we have Debye scattering curves for three kinds of chemical species, that is, $iso$-BiI$_2$-I, BiI$_2$•, and I$_2$, and therefore, in principle, three significant LSVs should be obtained. In Figure S6(e), there are a total of five significant LSVs, two of which correspond to two different solvent contributions, $(\partial S(q)/\partial T)_\rho$ and $(\partial S(q)/\partial \rho)_T$ multiplied by temperature and density changes, respectively. The LSVs from the theoretical data contain some noise because the $(\partial S(q)/\partial T)_\rho$ and $(\partial S(q)/\partial \rho)_T$ terms are from experimentally measured heating signals. In contrast, the LSVs from the experimental data shown in Figure S6(d) have only one meaningful LSV whose shape is just the same as the theoretical LSV1. We attribute this to the experimental noise in the high-$q$ region. To verify

this assignment, we generated mock data shown in Figure S6(c) by adding to theoretical data shown in Figure S6(b) the random noise derived from Gaussian distributions, whose mean values and standard deviations are the intensities of theoretical data shown in Figure S6(b) and the standard deviations of raw experimental data at each $q$-point, respectively. The LSVs obtained from this mock data are shown in Figure S6(f) and we can indeed see that there is only one significant LSV and the other LSVs are obscured beneath the noise floor. To further check the influence of the magnitude of noise, we have generated a set of mock data by the same method but with reduced standard deviations. The resultant mock data are shown in Figure S7. Within the shown trials, we were not able to retrieve the entire three solute-related LSVs, which were resolved in the LSVs of pure theoretical data in Figure S6(e). Instead, the second meaningful LSV, as shown in Figures S6(b) and S6(c), start to appear in the mock data generated using the standard deviations scaled by 0.5 and 0.6 with respect to the original experimental standard deviations, respectively.

## 6. Polychromatic correction

The X-ray pulse used in the experiment has a finite energy bandwidth of ~0.9%. In order to take into account this polychromaticity of the X-ray spectrum, all of the theoretical scattering intensities, $S(q)$, have been corrected by convoluting the X-ray spectrum as follows:

$$S(2\theta) = \frac{\int S_{\text{mono}}(2\theta)P(\lambda)\mathrm{d}\lambda}{\int P(\lambda)\mathrm{d}\lambda} \tag{S6}$$

where $S(2\theta)$ is the theoretical scattering intensity as a function of scattering angle $2\theta$ for a monochromatic X-ray beam and $P(\lambda)$ is the experimental X-ray spectrum from the U17 undulator.[S13]

## 7. DFT-optimized vs. experimentally determined structures of BiI₃, BiI₂· and *iso*-BiI₂–I

To address the disagreement between DFT-optimized and global-fit structures of reactants and photoproducts, we have examined the dependence of the optimized molecular structures on DFT functional and the solvent. The geometries of ground-state BiI₃, *iso*-BiI₂-I and BiI₂· were optimized using various DFT functionals with different basis sets. For comparison, the geometries were optimized using Hartree-Fock (HF) and Coupled-Cluster Singles and Doubles

(CCSD) methods as well. The numbers next to the I symbol are labels used to distinguish individual iodine atoms, as shown in Table S1. The geometric parameters for DFT-optimized $BiI_3$, *iso*-$BiI_2$-I and $BiI_2$· structures are summarized in Table S1. For the structure of $BiI_3$, the DFT-optimized geometries reproduce the experimentally determined geometry decently, although all calculated Bi-I bond lengths are longer than the experimentally determined value, 2.816 Å. In specific, the Bi-I bond lengths of the CCSD-optimized structure, 2.819 Å, show the best agreement with the experimental value. The deviations of calculated Bi-I bond lengths from the experimental values are less than 0.05 Å. Similarly, in the DFT-optimized structure of $BiI_2$·, Bi-I bond lengths are overestimated regardless of DFT functionals and basis sets.

The DFT-optimized geometries of *iso*-$BiI_2$-I, however, are significantly affected by DFT functionals and basis sets. The calculated geometric parameters are summarized in Table S1. Similar to the calculated Bi-I bond lengths in $BiI_3$, all DFT-calculated Bi-I1(-I2) and I2-I3 bond lengths are longer than the experimental values. The optimized geometry using B3LYP/dhf-TZVP shows the best agreement with the I2-I3 bond length, whereas the Bi-I1 bond lengths are 0.1 Å longer than the experimental values. On the other hand, the optimized geometry using CAM-B3LYP/def2-TZVP predict the Bi-I2 and Bi-I2 bond lengths within the deviation of 0.05 Å, but the I2-I3 bond length is longer by 0.278 Å than the experimental I2-I3 bond length. Other geometric parameters for defining the position of I3, Bi-I2-I3 angle and I1-Bi-I2-I3 dihedral angle, are also significantly affected by the DFT functionals and basis sets as shown in Table S1. In particular, all DFT-calculated I1-Bi-I2 angles are around 175°, except for the optimized geometries using B3LYP/dhf-TZVP and B3LYP/dhf-TZVPP. Also, even the CCSD-optimized geometry displays longer I2-I3 bond length, 3.784 Å, and the Bi-I2-I3 bond angle of 178.0°.

This discrepancy between DFT-optimized structures of $BiI_3$ and *iso*-$BiI_2$-I and their global-fit structures might be attributed to three factors of the calculations: (i) insufficient consideration of the spin-orbit coupling (SOC) effect, (ii) the limit of single reference DFT to describe the multi-reference characters, and (iii) the use of implicit solvation model. In other words, to predict the structure of *iso*-$BiI_2$-I more accurately, the SOC effect and multireference calculation methods must be included in the calculation since *iso*-$BiI_2$-I species consists of heavy atoms and is expected to have the mixed biradical and ionic characters like *iso*-$CHBr_2$-Br and *iso*-$CH_2I$-I.[S14] In addition, the use of implicit solvent model, conductor-like continuum model (CPCM), seems to be not enough to depict sophisticated solvation effects surrounding

*iso*-BiI$_2$-I. Indeed, the structural parameters of *iso*-BiI$_2$-I is most likely to be affected by the surrounding solvent molecules since the potential energy surface of *iso*-BiI$_2$-I is broad and shallow like that in *iso*-CHI$_2$-I. To evaluate solvent dependence of the *iso*-BiI$_2$-I geometry, we optimized the geometries of *iso*-BiI$_2$-I in various solvent fields. The result is shown in Table S2. As the solvent polarity increases, the Bi-I1 bond length of *iso*-BiI$_2$-I gradually decreases from 2.785 to 2.732 Å, while the Bi-I bond length of BiI$_3$ increases from 2.800 Å to 2.824 Å. Moreover, the I2-I3 bond length of *iso*-BiI$_2$-I in acetonitrile, 3.772 Å, is 0.664 Å longer than that in cyclohexane and the Bi-I2-I3 angle of *iso*-BiI$_2$-I in acetonitrile is 175.1°, while the Bi-I2-I3 angle in cyclohexane, 123.2°, is much smaller than those in other polar solvents. This result implies that the geometry of *iso*-BiI$_2$-I is also significantly affected by the solvent environment in addition to the DFT functionals and basis sets. Meanwhile, the barrier height for the back isomerization from *iso*-BiI$_2$-I to BiI$_3$ (Ea) and the relative energy of *iso*-BiI$_2$-I (ΔE) are largely influenced by the solvent field, whereas the relative energy of dissociation fragments (BiI$_2$· + I·), ΔE(dissociation), is insensitive to the choice of solvent field, as shown in Table S2. For example, in acetonitrile, the relative energy of *iso*-BiI$_2$-I (ΔE) and its barrier height (Ea), 0.06 and 1.73 eV, are smaller than those in cyclohexane, 0.19 and 2.21 eV, while the relative energy of dissociation fragments (BiI$_2$· + I·), 2.12 eV, is similar to that in cyclohexane, 2.09 eV. Thus, the calculation result supports that the relaxation of *iso*-BiI$_2$-I to BiI$_3$ is more favored than the radical dissociation channel in the polar solvent environment.

## 8. References

(S1) Wulff, M.; Kong, Q. Y.; Cammarata, M.; Lo Russo, M.; Anfinrud, P.; Schotte, F.; Lorenc, M.; Ihee, H.; Kim, T. K.; Plech, A. Picosecond diffraction at the ESRF: How far have we come and where are we going? *AIP Conf. Proc.* **2007**, *879*, 1187.

(S2) Christensen, M.; Haldrup, K.; Bechgaard, K.; Feidenhans'l, R.; Kong, Q. Y.; Cammarata, M.; Lo Russo, M.; Wulff, M.; Harrit, N.; Nielsen, M. M.; Am, J.; Kim, T. K.; Lee, J. H.; Wulff, M.; Kong, Q.; Ihee, H. Spatiotemporal Kinetics in Solution Studied by Time-Resolved X-Ray Liquidography (Solution Scattering). *ChemPhysChem* **2009**, *10*, 3140.

(S3) James, F.; Roos, M. Minuit - System for Function Minimization and Analysis of Parameter Errors and Correlations. *Comput. Phys. Commun.* **1975**, *10*, 343.

(S4) Cammarata, M.; Lorenc, M.; Kim, T. K.; Lee, J. H.; Kong, Q. Y.; Pontecorvo, E.; Lo Russo, M.; Schiro, G.; Cupane, A.; Wulff, M.; Ihee, H. Impulsive solvent heating probed by picosecond x-ray diffraction. *J. Chem. Phys.* **2006**, *124*.

(S5) Cances, E.; Mennucci, B.; Tomasi, J. A new integral equation formalism for the polarizable continuum model: Theoretical background and applications to isotropic and anisotropic dielectrics. *J. Chem. Phys.* **1997**, *107*, 3032.

(S6) Frisch, M. J.; Trucks, G. W.; Schlegel, H. B.; Scuseria, G. E.; Robb, M. A.; Cheeseman, J. R.; Scalmani, G.; Barone, V.; Petersson, G. A.; Nakatsuji, H. *et al*. Gaussian 16 Rev. B.01. *Gaussian, Inc., Wallingford CT* **2016**.

(S7) Refson, K. Moldy: a portable molecular dynamics simulation program for serial and parallel computers. *Comput. Phys. Commun.* **2000**, *126*, 310.

(S8) Rappe, A. K.; Casewit, C. J.; Colwell, K. S.; Goddard, W. A.; Skiff, W. M. Uff, a Full Periodic-Table Force-Field for Molecular Mechanics and Molecular-Dynamics Simulations. *JACS* **1992**, *114*, 10024.

(S9) Hoover, W. G. Canonical Dynamics - Equilibrium Phase-Space Distributions. *Phys. Rev. A* **1985**, *31*, 1695.

(S10) Henry, E. R.; Hofrichter, J. Singular Value Decomposition - Application to Analysis of Experimental-Data. *Methods Enzymol.* **1992**, *210*, 129.

(S11) Henry, E. R. The use of matrix methods in the modeling of spectroscopic data sets. *Biophys. J.* **1997**, *72*, 652.

(S12) Kim, K. H.; Oang, K. Y.; Kim, J.; Lee, J. H.; Kim, Y.; Ihee, H. Direct observation of myoglobin structural dynamics from 100 picoseconds to 1 microsecond with picosecond X-ray solution scattering. *Chem. Commun.* **2011**, *47*, 289.

(S13) Ihee, H.; Wulff, M.; Kim, J.; Adachi, S. Ultrafast X-ray scattering: structural dynamics from diatomic to protein molecules. *Int. Rev. Phys. Chem.* **2010**, *29*, 453.

(S14) Borin, V. A.; Matveev, S. M.; Budkina, D. S.; El-Khoury, P. Z.; Tarnovsky, A. N. Direct photoisomerization of $CH_2I_2$ vs. $CHBr_3$ in the gas phase: a joint 50 fs experimental and multireference resonance-theoretical study. *Phys. Chem. Chem. Phys.* **2016**, *18*, 28883.

**Table S1**. Comparison of DFT optimized structures of ground-state BiI$_3$, *iso*-BiI$_2$-I and BiI$_2$·. The CPCM solvation model is used for the geometry optimization to take into account the solvent effect of acetonitrile. HF and CCSD calculations were carried out for comparison. The units for the bond lengths and angles are Å and degree, respectively.



BiI$_3$   *iso*-BiI$_2$-I   BiI$_2$
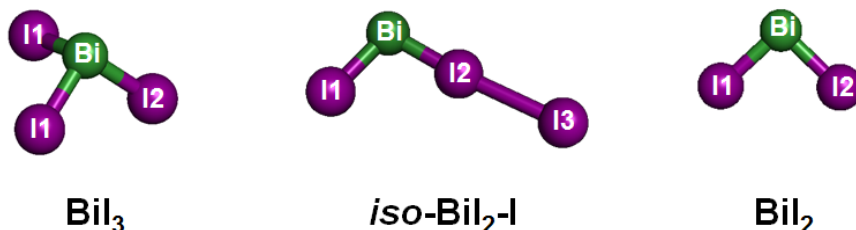
| Geometric parameters | B3LYP /dhf-TZVP | B3LYP /dhf-TZVPP | CAM-B3LYP /dhf-TZVP | CAM-B3LYP /def2-TZVP | ω97XD /def2-TZVP | MN12-SX /def2-TZVP | M06-2X /def2-TZVP | UHF /def2-TZVP | CCSD/ /def2-TZVP | Experiment |
|---|---|---|---|---|---|---|---|---|---|---|
| **BiI$_3$** | | | | | | | | | | |
| Bi-I1 | 2.864 | 2.861 | 2.830 | 2.824 | 2.828 | 2.821 | 2.825 | 2.843 | 2.819 | 2.816 |
| Bi-I2 | 2.865 | 2.862 | 2.832 | 2.826 | 2.829 | 2.822 | 2.826 | 2.845 | 2.818 | 2.816 |
| I1-I2 | 4.369 | 4.363 | 4.282 | 4.272 | 4.274 | 4.238 | 4.251 | 4.284 | 4.238 | 4.258 |
| I1-I1 | 4.377 | 4.372 | 4.287 | 4.275 | 4.277 | 4.238 | 4.251 | 4.286 | 4.239 | 4.258 |
| I1-Bi-I2 | 99.4 | 99.3 | 98.3 | 98.2 | 98.1 | 97.4 | 97.6 | 97.7 | 97.5 | 98.2 (fixed) |
| I1-Bi-I1 | 99.6 | 99.6 | 98.5 | 98.4 | 98.3 | 97.4 | 97.6 | 97.8 | 97.5 | 98.2 (fixed) |
| ***iso*-BiI$_2$-I** | | | | | | | | | | |
| Bi-I1 | 2.799 | 2.788 | 2.741 | 2.732 | 2.734 | 2.733 | 2.737 | 2.745 | 2.730 | 2.688 |
| Bi-I2 | 2.757 | 2.753 | 2.732 | 2.723 | 2.724 | 2.720 | 2.726 | 2.740 | 2.719 | 2.679 |
| I1-I2 | 4.313 | 4.301 | 4.226 | 4.210 | 4.203 | 4.167 | 4.158 | 4.194 | 4.156 | 4.193 |
| I2-I3 | 3.460 | 3.540 | 3.669 | 3.722 | 3.776 | 3.729 | 3.700 | 5.089 | 3.784 | 3.444 |
| Bi-I2-I3 | 137.4 | 141.5 | 175.5 | 175.1 | 175.1 | 175.5 | 178.6 | 164.9 | 178.0 | 127.2 |
| I1-Bi-I2 | 101.9 | 101.8 | 101.0 | 101.0 | 100.7 | 99.7 | 99.1 | 99.7 | 99.4 | 102.7 |
| I1-Bi-I2-I3 | -93.0 | -93.9 | -147.3 | -142.0 | -137.3 | -98.4 | -171.0 | 134.6 | -129.8 | -64.9 |
| **BiI$_2$·** | | | | | | | | | | |
| Bi-I1(I2) | 2.856 | 2.853 | 2.826 | 2.820 | 2.819 | 2.805 | 2.832 | 2.858 | 2.818 | 2.778 |
| I1-I2 | 4.393 | 4.387 | 4.305 | 4.294 | 4.290 | 4.244 | 4.282 | 4.328 | 4.258 | 4.050 |
| I1-Bi-I2 | 100.6 | 100.5 | 99.2 | 99.2 | 99.1 | 98.3 | 98.2 | 98.4 | 98.1 | 93.6 |

**Table S2.** The geometrical parameters of DFT-optimized $BiI_3$ and *iso*-$BiI_2$-I structures. All geometries are optimized using CAM-B3LYP/def2-TZVP with CPCM implicit solvation model. The Ea indicate the barrier height for the back isomerization from the *iso*-$BiI_2$-I to $BiI_3$, and ΔE and ΔE(dissociation) represent the relative energies of the *iso*-$BiI_2$-I and dissociation fragments ($BiI_2$· + I·) compared to that of $BiI_3$. ε is the dielectric constant of the solvent. The units for the energy, bond lengths and angles are eV, Å and degree, respectively. N/A: not available.
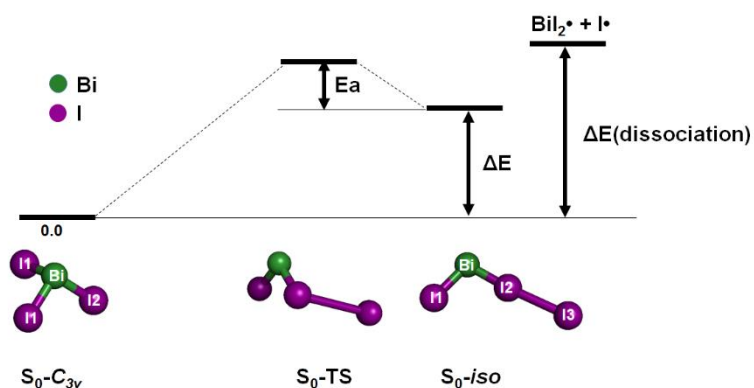


| Parameters | Gas phase | Cyclohexane (ε=2.02) | DCM (ε=8.93) | Ethanol (ε=24.5) | Methanol (ε=32.7) | Acetonitrile (ε=37.5) | Experiment |
|---|---|---|---|---|---|---|---|
| Ea | 0.29 | 0.19 | 0.09 | 0.07 | 0.06 | 0.06 | N/A |
| ΔE | 2.24 | 2.21 | 1.92 | 1.76 | 1.74 | 1.73 | N/A |
| ΔE(dissociation) | 2.08 | 2.09 | 2.11 | 2.12 | 2.12 | 2.12 | N/A |
| **$S_0$-$C_{3V}$** | | | | | | | |
| Bi-I1 | 2.800 | 2.810 | 2.821 | 2.824 | 2.824 | 2.824 | 2.816 |
| Bi-I2 | 2.800 | 2.810 | 2.822 | 2.825 | 2.826 | 2.826 | 2.816 |
| I1-I2 | 4.297 | 4.288 | 4.275 | 4.273 | 4.272 | 4.272 | 4.258 |
| I1-I1 | 4.299 | 4.290 | 4.279 | 4.276 | 4.275 | 4.275 | 4.258 |
| I1-Bi-I2 | 100.2 | 99.5 | 98.5 | 98.3 | 98.3 | 98.2 | 98.2(fixed) |
| I1-Bi-I1 | 100.3 | 99.5 | 98.6 | 98.4 | 98.4 | 98.4 | 98.2(fixed) |
| **$S_0$-*iso*** | | | | | | | |
| Bi-I1 | 2.785 | 2.786 | 2.735 | 2.733 | 2.732 | 2.732 | 2.688 |
| Bi-I2 | 2.723 | 2.704 | 2.720 | 2.722 | 2.722 | 2.723 | 2.679 |
| I1-I2 | 4.275 | 4.256 | 4.222 | 4.212 | 4.210 | 4.210 | 4.193 |
| I2-I3 | 2.953 | 3.058 | 3.546 | 3.695 | 3.717 | 3.722 | 3.444 |
| Bi-I2-I3 | 121.1 | 123.2 | 175.6 | 175.2 | 175.1 | 175.1 | 127.2 |
| I1-Bi-I2 | 101.8 | 101.6 | 101.4 | 101.1 | 101.0 | 101.0 | 102.7 |
| I1-Bi-I2-I3 | -90.4 | -90.9 | -148.6 | -144.5 | -141.8 | -142.0 | -64.9 |
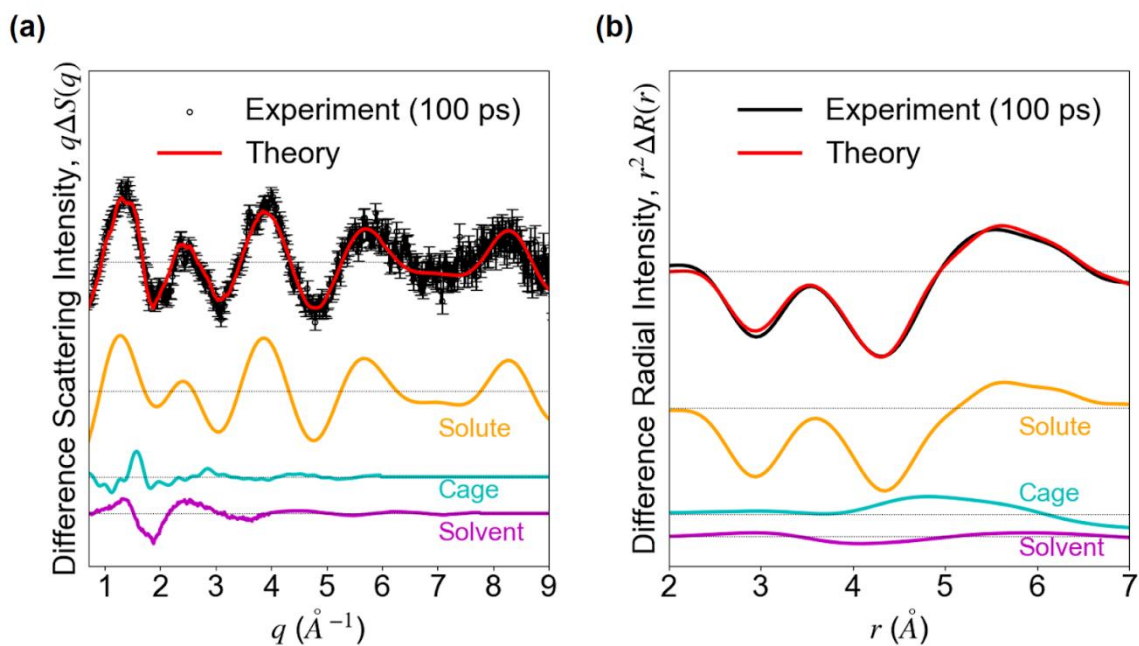
**Figure S1.** Signal contributions of the solute, cage and solvent to (a) the total difference scattering signal and (b) the radial intensity at 100 ps. The experimental difference scattering is shown with black dots with error bars. The solute, cage and solvent contributions extracted from the theoretical curve (red solid line) are shown in orange, cyan and magenta solid curves, respectively.
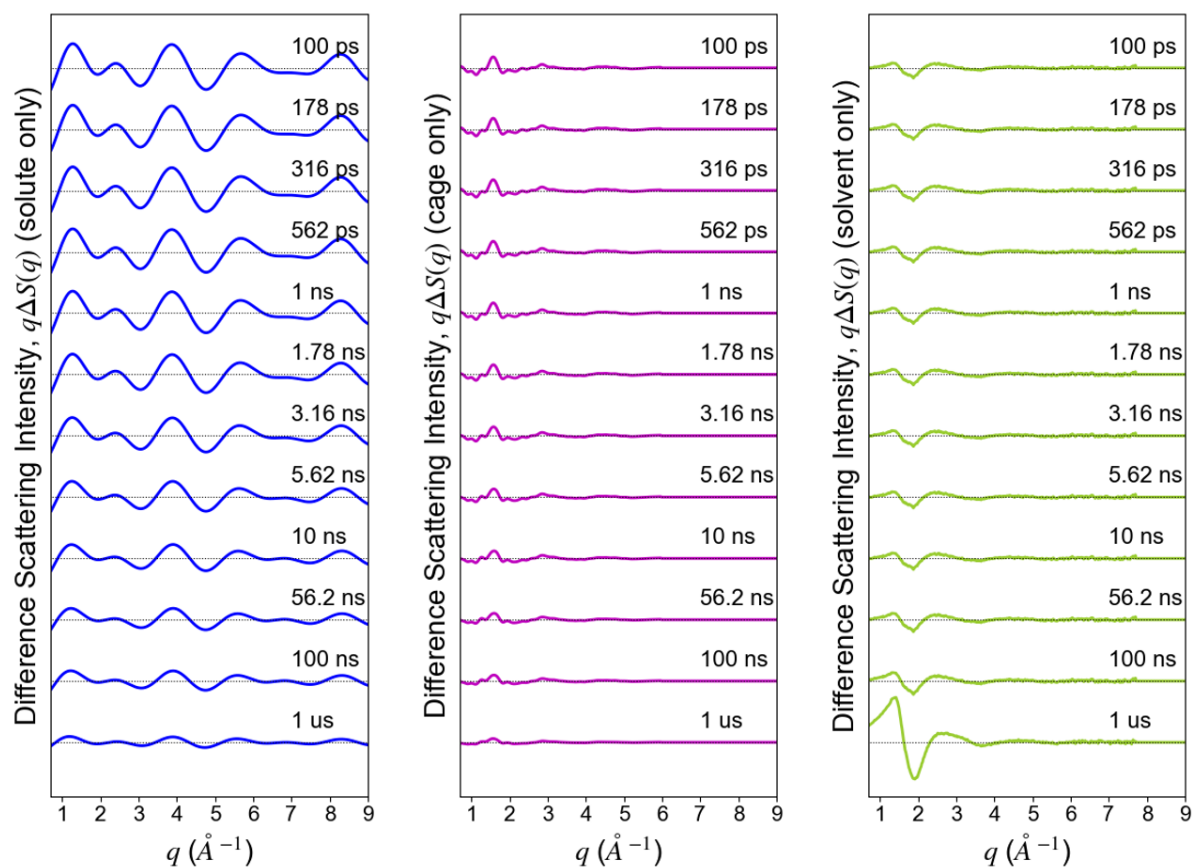
**Figure S2.** Decomposed theoretical TRXL signals, $q\Delta S(q)$. Blue curves on the left, magenta curves on the middle and green curves on the right represent the solute-only, cage (solute-solvent cross term) and solvent-only contributions, respectively. All three panels are on the same scale.
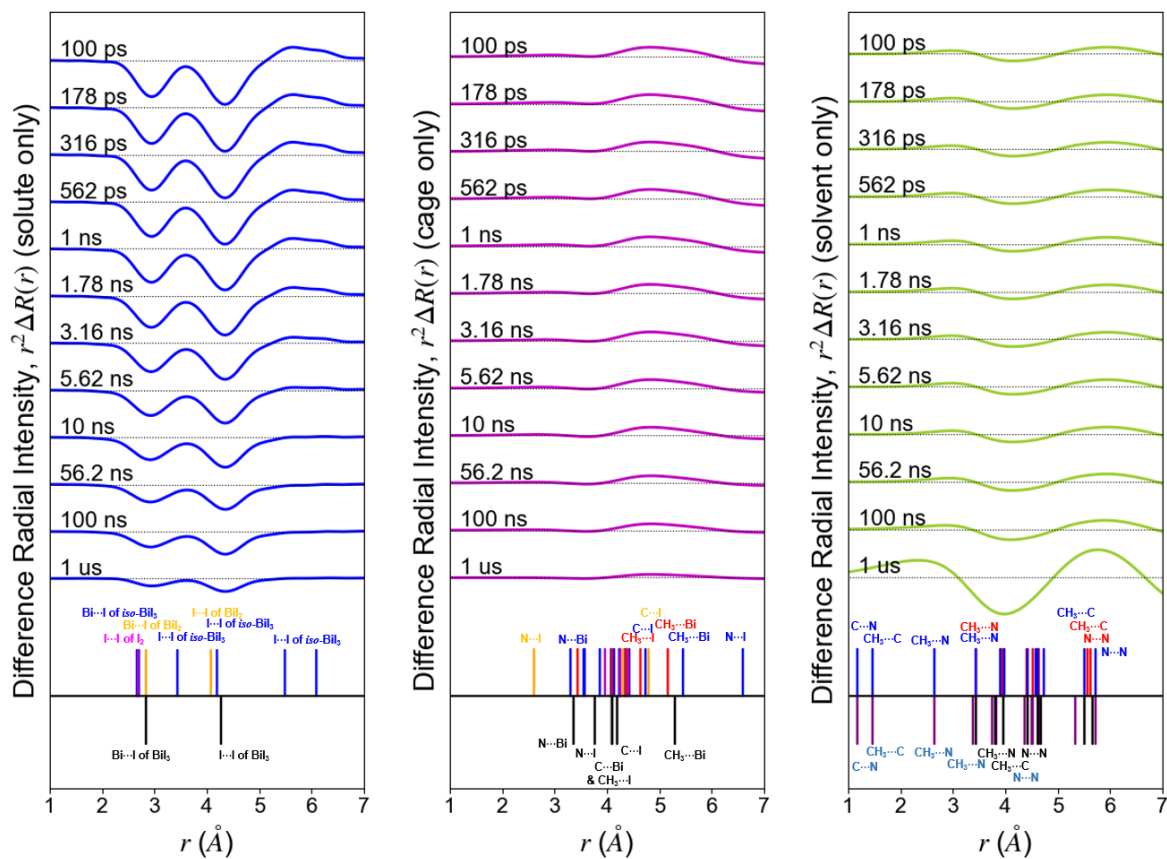
**Figure S3.** Decomposed theoretical difference radial intensities, $r^2 \Delta R(r)$, obtained by sine-Fourier transform of $q\Delta S(q)$ signals shown in Figure S2. Blue curves on the left, magenta curves on the middle and green curves on the right represent the solute-only, cage (solute-solvent cross term) and solvent-only contributions of $r^2 \Delta R(r)$, respectively. All three panels are on the same scale. The upward and downward bars represent the newly formed and depleted interatomic pair distances, respectively. The pair distances related to $BiI_3$, $iso$-$BiI_3$, $BiI_2$· and $I_2$ are shown in black, blue, orange and magenta, respectively. For solute-only $r^2 \Delta R(r)$ curves, all of the assigned pair distances are shown. For cage and solvent-only $r^2 \Delta R(r)$, some representative assigned pair distances among all pair distances within $1 \sim 7$ Å indicated with vertical bars, which mainly contribute to the signals, are shown. In the case of solvent-only $r^2 \Delta R(r)$, the bars in red and black represent the newly formed and depleted pair distances, respectively, due to the temperature rise whereas the bars in blue and purple indicate the newly generated and depleted pair distances, respectively, originating from the density decrease.
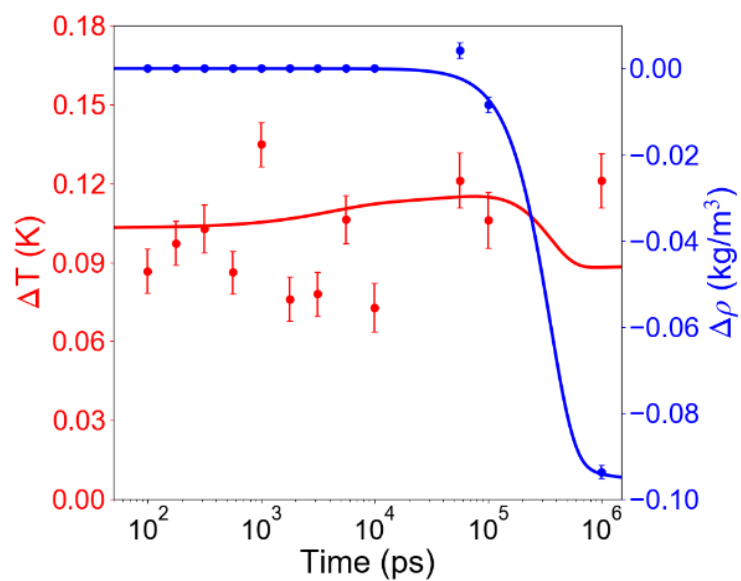
**Figure S4.** Temperature (red) and density (blue) changes of solvent induced by photoexcitation of $BiI_3$ in acetonitrile. Solid lines were obtained by solving hydrodynamics equations during the global analysis and dots with error bars were obtained from fitting the experimental difference scattering curve at each time delay individually by a linear combination of necessary contributions where the temperature and density changes for each time delay were included in fit parameters.
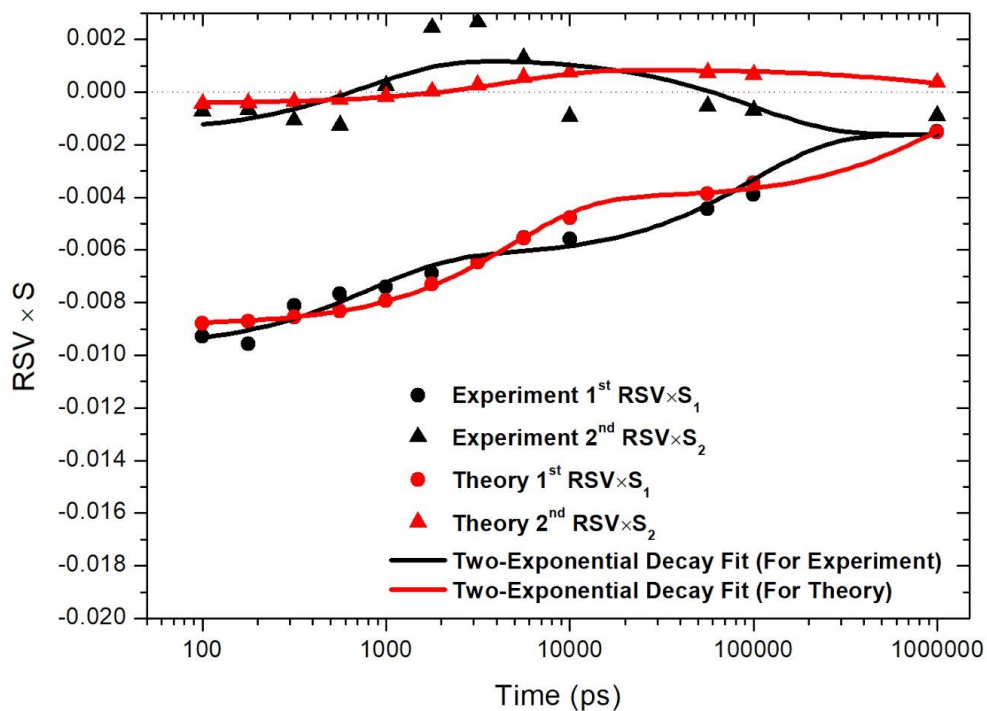
**Figure S5.** Right singular vectors (RSVs) weighted by singular values (S) obtained from singular vector decomposition (SVD) of the experimental (black circles and triangles) and the noise-free theoretical (red circles and triangles) difference scattering intensities, $q\Delta S$, at high-$q$ region ($q = 4.0 \sim 9.0$ Å$^{-1}$), where the solute-related contributions are dominant. Fit curves using linear combination of two exponential functions are shown for experimental RSVs in black solid lines and theoretical RSVs in red solid lines, respectively.
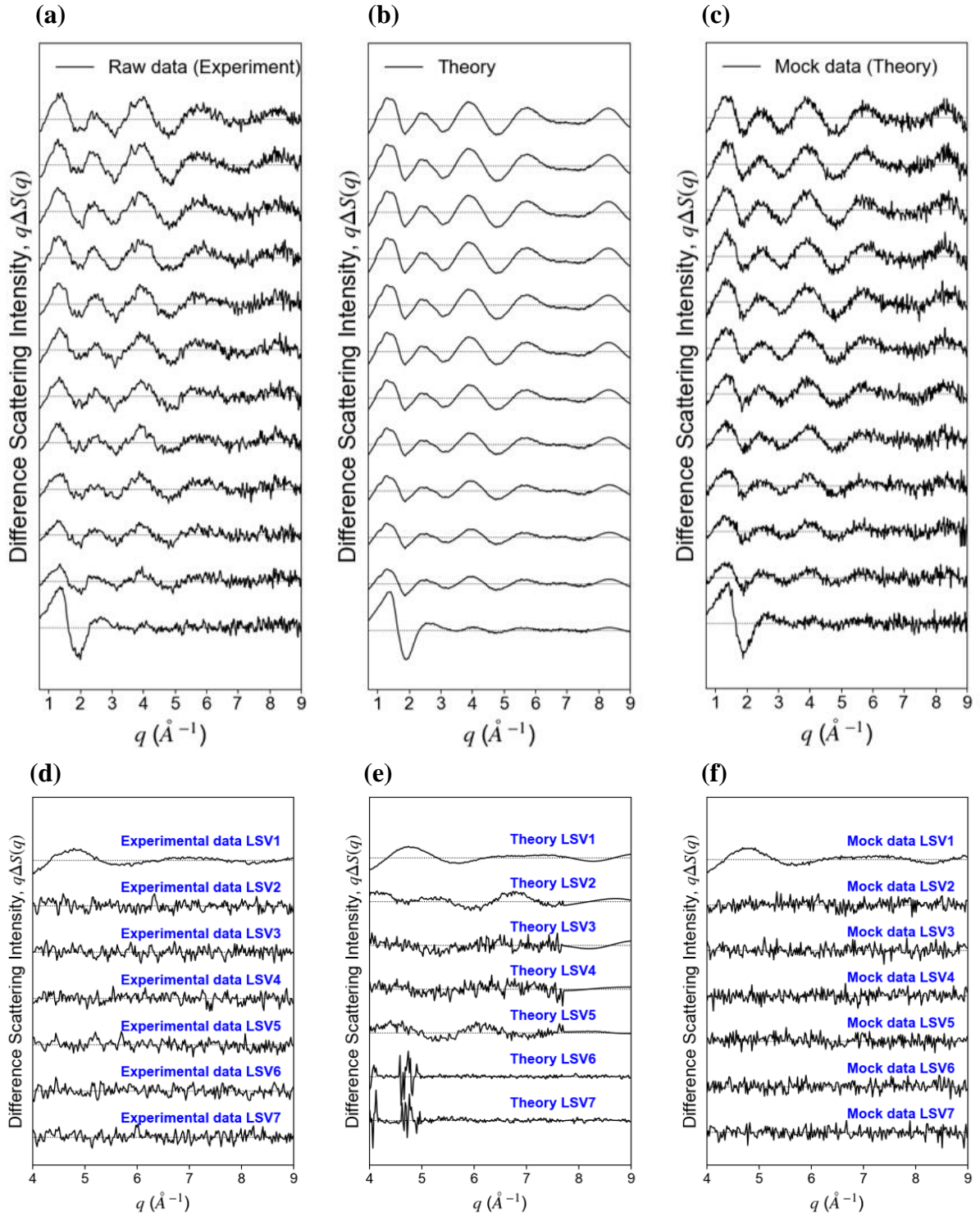
**Figure S6.** (a) Raw experimental data, (b) theoretical data obtained from global fit analysis and (c) mock data generated by adding to the theoretical data shown in (b) random noise derived from Gaussian distributions whose mean values and standard deviations are the intensities of theoretical data shown in (b) and the standard deviations of raw experimental data at each $q$-point, respectively. (d) The LSVs obtained from SVD of raw experimental data, (e) LSVs for the theoretical data and (f) LSVs for the mock data at a $q$-range of $4.0 \sim 9.0$ Å$^{-1}$.
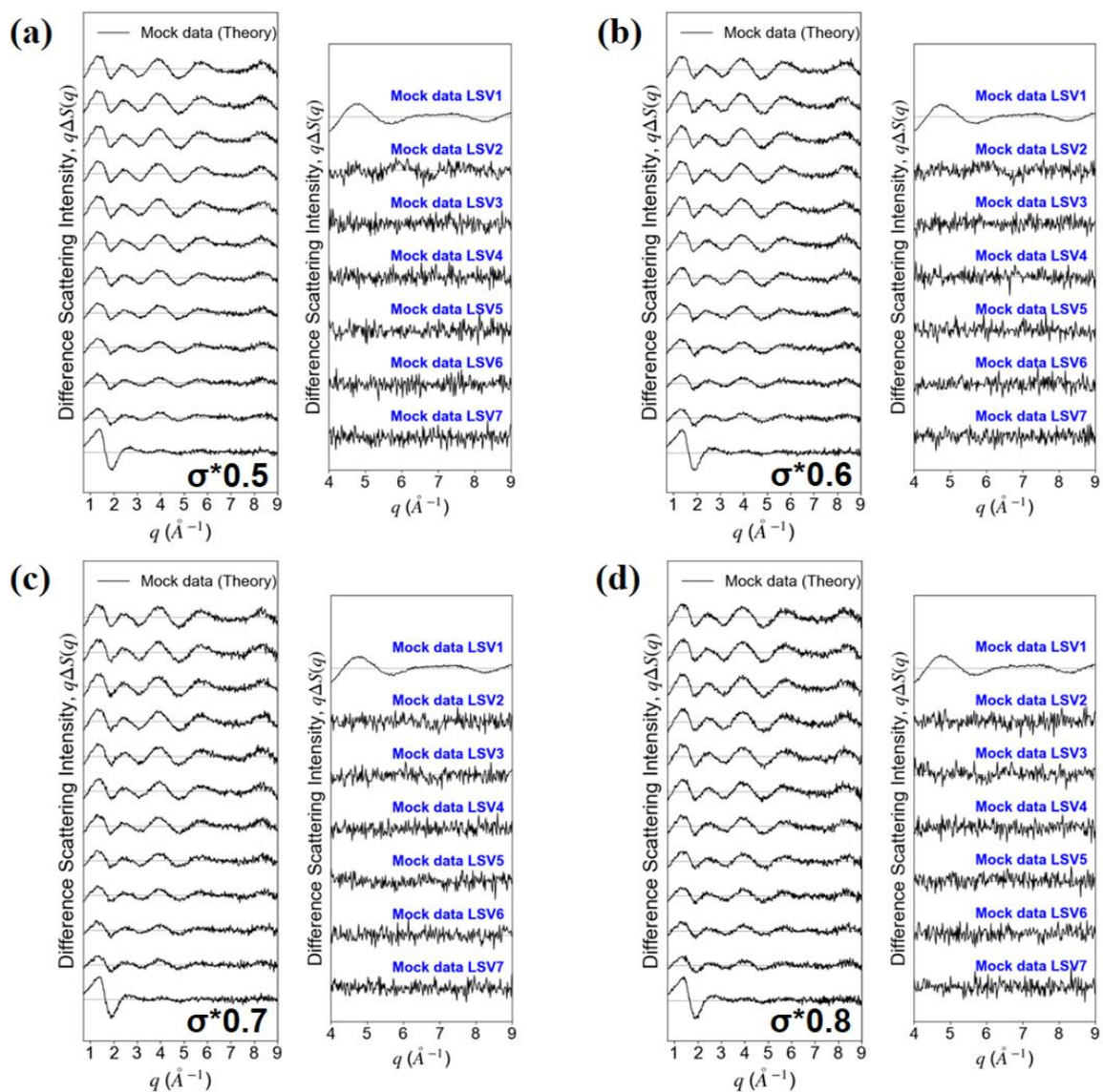
**Figure S7.** LSVs for the mock data generated by the same method used in Figure S6 but with reduced standard deviations by a factor of (a) 0.5, (b) 0.6, (c) 0.7 and (d) 0.8.